Soft Matter

Accepted Manuscript

This is an *Accepted Manuscript*, which has been through the Royal Society of Chemistry peer review process and has been accepted for publication.

Accepted Manuscripts are published online shortly after acceptance, before technical editing, formatting and proof reading. Using this free service, authors can make their results available to the community, in citable form, before we publish the edited article. We will replace this *Accepted Manuscript* with the edited and formatted *Advance Article* as soon as it is available.

You can find more information about *Accepted Manuscripts* in the Information for Authors.

Please note that technical editing may introduce minor changes to the text and/or graphics, which may alter content. The journal's standard Terms & Conditions and the Ethical guidelines still apply. In no event shall the Royal Society of Chemistry be held responsible for any errors or omissions in this *Accepted Manuscript* or any consequences arising from the use of any information it contains.

ROYAL SOCIETY OF CHEMISTRY

www.rsc.org/softmatter

Soft Matter RSCPublishing

PAPER

Combined Epitaxial Self-Assembly of the Block Copolymer Lamellae on Hexagonal Prepattern within Microgroove

Cite this: DOI: 10.1039/x0xx00000x

Received 00th January 2012,
Accepted 00th January 2012

DOI: 10.1039/x0xx00000x

www.rsc.org/

Hyunjung Jung,[a] Sanghoon Woo,[a] Sungmin Park,[b] Sumi Lee,[c] Minhyuk Kang,[c] Youngson Choe,[d] Jeong Gon Son,[e] Du Yeol Ryu,[b] June Huh*[a] and Joona Bang*[a]

Directed self-assembly (DSA) of block copolymers (BCPs) has emerged as an excellent alternative method to replace or complement the conventional photolithography, due to their ~10 nm scale of microdomain ordering, the variety of microstructures, and compatibility with current lithographic process. In DSA, BCP microdomains are controlled via guide patterns, and two main techniques are popular; graphoepitaxy and chemoepitaxy. In this work, we demonstrate the simple and feasible technology for DSA process by combining the graphoepitaxy with “inexpensive” chemoepitaxial assembly to improve the alignment of lamellar microdomains. For the chemoepitaxial assembly, the hexagonal surface patterns from crosslinkable, cylinder-forming BCP were employed as a guiding assistance to the graphoepitaxial assembly of overlaying BCP lamellar film. When the guiding patterns were prepared on the hexagonal patterns, it was found that the degree of lamellar alignment is significantly improved compared to the lamellar alignment on the homogeneous neutral layers. The simulation results suggest that the underlying hexagonal pattern can assist the lamellar alignment by reducing a large number of orientational states of lamellar layers. This strategy can be applicable to various nanofabrication processes that require a high degree of fidelity in controlling nanopatterns over large area with reduced cost.

Introduction

Block copolymer (BCP) lithography has been considered as promising candidates for the fabrication of nanopatterns and has the potential to integrate into current manufacturing processes such as conventional photolithography, due to its cost effective and high throughput nature.[1-4] The resulting BCP patterns have been used in various applications including microelectronics, nanoreactors for nanoparticle/nanowire fabrication, nanoporous membranes, etc.[5-9] In this case, significant efforts have been devoted to control the orientation and the lateral ordering of BCP microdomains. On the flat and untemplated substrates, the orientation of BCP microdomains can be controlled but the lateral ordering is inherently limited by grain defects, preventing their applications where addresability is desired.[10-12]

To overcome these limitations, directed self-assembly (DSA) of BCP thin films has been employed to achieve a defect-free, long-ranged ordering of microdomains. Two popular approaches for DSA of BCP nanopatterns include a use of chemically patterned surfaces and a graphoepitaxy with topographic patterns.[13-16] As preceding examples, Kramer and coworkers demonstrated that the BCP microdomains can be effectively aligned within topographical trenches or hexagon-shaped wells.[17, 18] The guide patterns for graphoepitaxy can be readily fabricated by conventional photolithography process. Many groups have developed this methods further to employ various kinds of BCPs or different types of topographic patterns (e.g, photoresist patterns, imprinted patterns, etc).[19, 20] The ordering of BCP microdomains within trenches is mainly governed by commensurability and interaction of each block with substrates, and many studies have focused on the enhancement of BCP ordering by adjusting the various experimental variables, such as width of trenches, molecular weight of BCPs, film thicknesses, annealing conditions, etc.[21-27] However, it is well known that the effect of confined geometry diminishes as the distance from the sidewall is increased, indicating the width of trench is an inherent limitation in graphoepitaxy technique.[28, 29] To overcome this limitation, an additional tool, such as chemoepitaxial assembly, is introduced to pattern the substrate on length scale similar to BCP microdomains.[30]

In this regards, Nealey and coworkers prepared the chemically patterned surface to direct the self-assembly of BCP microdomains.[31-34] In addition to simple line or dot patterns, they further demonstrated that various nonregular shapes or sparse patterns can also successfully guide the BCP microdomains into desired patterns.[35, 36] However, the major drawback of this technique is that the surface should be precisely prepatterned to have the same (or similar) length scale as overlying BCP microdomains using costly and complicated lithographic steps such as extreme UV lithography,[31-33] e-beam

Soft Matter Accepted Manuscript

lithography,[34-36] or immersion lithography.[37-39] In this vein, Ruiz and coworkers demonstrated that the crosslinked, horizontally oriented cylinders that were prepared within lithographic trenches can effectively aligned lamellar films due to the registration between top lamellar pattern and the underlying cylinder template.[15] Later, Kim and coworkers further extended this system to fabricate highly oriented lamellar patterns over large area.[16] In this system, the alignment of lamellae films is determined by underlying cylinder patterns. The monolayer of parallel cylinders is spin cast onto the trench patterns and thermally annealed to form highly aligned cylinder prepatterns. Since these cylinder patterns are aligned by graphoepitaxial assembly induced by sidewall, it can be expected that the effect of sidewall diminishes as the distance from the sidewall is increased. Whilst these preceding examples successfully demonstrated the improvement on the feasibility and processability of either graphoepitaxy or chemoepitaxy, it would be also highly desirable if one can develop a protocol that can integrate the advantages of these two techniques into one process.

We previously designed the crosslinkable poly(styrene-*b*-methyl methacrylate) (PS-*b*-PMMA) BCP to fabricate the three-dimensional multilayered structures showing the perpendicular-oriented lamellae on top of the underlying crosslinked cylindrical layer exhibiting perpendicular orientation of microdomains.[40] In this case, it was shown that the PMMA lamellae are in good registration with the underlying PMMA cylinders due to the minimization of unfavorable wetting interactions at the interface of BCP films, suggesting the possibility that these BCP patterns can be used as "inexpensive" chemoepitaxial assembly surfaces. In this work, we demonstrate that chemoepitaxial assembly via pre-existing BCP hexagonal patterns on the substrate can be effectively combined with graphoepitaxy technique to further improve the lateral alignment of BCP lamellar domains. On the hexagonal prepatterns of crosslinked cylinder-forming PS-*b*-PMMA BCP films showing the perpendicular orientation of PMMA cylinders, the microgroove patterns were fabricated via conventional photolithography process. Then we applied two PS-*b*-PMMA lamellae having the similar domain spacing with underlying cylindrical BCP patterns. Consequently, it was found that the alignment of lamellae with pre-existing BCP patterns is significantly enhanced compared to the case where no BCP patterns were employed on the surface within trenches.

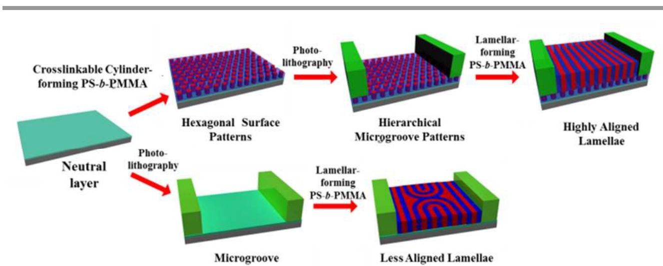

Scheme 1. Schematic illustration of the experimental setup for the combined chemoepitaxial/graphoepitaxial assembly of lamella-forming BCPs on the hexagonal prepatterns within microgroove.

Results and discussion

Scheme 1 depicts the experimental setup for our combined epitaxial (chemoepitaxial/graphoepitaxial) assembly of BCP lamellae using hexagonal prepattern and trench geometry. For the underlying prepatterned layer, we synthesized the crosslinkable cylinder-forming PS-*b*-PMMA BCP via reversible addition fragmentation chain transfer (RAFT) polymerization by incorporating a small fraction of crosslinkable monomer in the styrene unit (3 mol % relative to styrene unit) (Fig. S1). As a crosslinkable unit, we used the Meldrum's acid based monomer reported previously, which can generate a highly reactive ketene group upon heating.[41, 42] The ketene group as a cross-linker has several advantages such as fast cross-linking reaction and high cross-linking temperature (> 200 ℃). In particular, the high cross-linking temperature of ketene group allow us to prepare well-ordered cylindrical morphology annealed below the cross-linking temperature when the annealing condition is properly chosen.[43] The number average molecular weight (M_n) of the crosslinkable PS-*b*-PMMA is 61 kg/mol (polydispersity index of 1.09), and the volume fraction of PMMA block was controlled to be 0.29 to ensure the cylindrical morphology. The hexagonally arrayed cylinders were prepared by thermal annealing of a crosslinkable PS-*b*-PMMA BCP on the neutral layer at 190 ℃ for 12 hours, and then thermally cross-linked at 250 ℃ for 10 min to render the prepatterned film stable. The principal domain spacing (λ_C) of the cylindrical prepattern after crosslinking is measured to be 33.7 nm. Subsequently, a trench geometry is constructed by introducing PMMA-selective sidewalls (SU-8) on the hexagonal prepattern using i-line photolithography process. The separation distance between the two adjacent sidewalls is 1.5-μm and the trench height is 250 nm. The lamella-forming PS-*b*-PMMA BCP was then spin-coated and subsequently annealed within the trench that has PMMA-selective sidewalls and hexagonally patterned (PMMA dots in PS matrix) bottom surface. The M_n's of lamella-forming, symmetric PS-*b*-PMMA BCPs on top of the hexagonal prepattern are 51 kg/mol ($f_{PS,volume}$ = 0.52) and 75 kg/mol ($f_{PS,volume}$ = 0.54) with the interlamellar spacing (λ_L) of 28.3 nm and 38.1 nm, respectively (Fig. S2). In fact, it is worth noting that the 2D hexagonal patterns were not directly spin casted within trenches to avoid the capillarity of underlying film near the sidewalls, which may affect the alignment of overlying lamellar film via additional, capillary-induced topographic effect. Instead, the hexagonal patterns were prepared before fabricating the trenches, and hence the (100) directions in the hexagonal patterns are not aligned along the sidewall and they are randomly oriented within trenches. Nevertheless, as will be discussed later, it was shown that randomly oriented hexagonal lattices can guide the overlying lamellae in three degenerate (100) directions and thus effectively compensate the decreased effect of sidewall.

We begin with discussing the effect of the underlying hexagonal pattern for guiding lamellar assembly in the absence of the sidewall. Fig. 1a presents the scanning electron microscopy (SEM) image of multilayer film where a lamellar film of PS-*b*-PMMA with M_n = 51 kg/mol is assembled on the hexagonal prepattern. The PMMA domains, removed by reactive ion etching after the assembly, appear dark in the SEM image. The morphology of the multilayer clearly shows that lamellar PMMA domains are positioned along the lines connecting between PMMA cylindrical dots, indicating the surface guidance effect of the prepattern on the lamellar assembly. It is worth pointing out that the PS/PMMA interfacial area at the boundary between lamellar and hexagonal layer gets a minimum when $\lambda_C = \lambda_L$ such that the lamellae can avoid unfavorable PS/PMMA contacts effectively by being aligned along (100) direction in Bravais-Miller hexagonal lattice. (Fig. 1b) As reported in our previous work, this process of minimizing interfacial energy as well as the entropy-type

Soft Matter Accepted Manuscript

This journal is © The Royal Society of Chemistry 2015

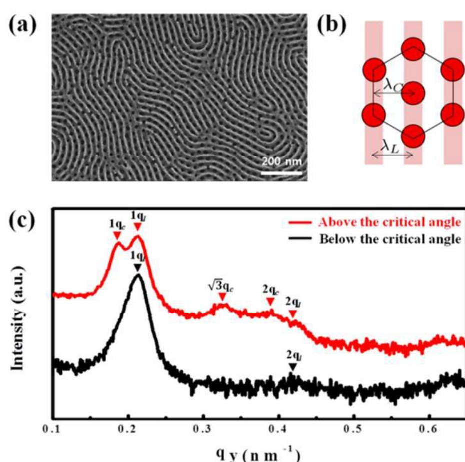

Fig. 1. (a) SEM image for 51 kg/mol PS-*b*-PMMA lamellae (thickness of ~20 nm) on the underlying hexagonal patterns from crosslinkable PS-*b*-PMMA cylinders (M_n = 61 kg/mol) after removing the PMMA microdomain; (b) Schematic representation of the ideal registration of lamellar domain on the underlying hexagonal pattern; (c) 1D GISAXS intensity profiles of lamellar/cylinder multilayer film on the neutral layer.

interaction originated from the negative line tension[44] or nematic interaction[45] give rise to the formation of lamellae perpendicular to the substrate, favoring it over lamellae parallel to the substrate.[40] Therefore, similar principal domain spacing between lamellar and hexagonal layer in this study, i.e., λ_C/λ_L = 1.19 for PS-*b*-PMMA with M_n = 51 kg/mol, and λ_C/λ_L = 0.88 for PS-*b*-PMMA with M_n = 75 kg/mol, can help the formation of lamellae orienting perpendicular to the substrate by locating PS and PMMA lamellar domains on their corresponding domains of the hexagonal morphology. Fig. 1c presents 1D grazing-incidence small-angle x-ray scattering (GISAXS) profile for the lamellae (M_n = 51 kg/mol) on the cylindrical layer. The double-peaked and the single-peaked GISAXS profiles, which were obtained at the scattering angle above and below a certain critical angle, support that the film is double-layers with two different principal domain spacing, which corresponds to 29.5 nm for the upper lamellar layer and 33.6 nm for the lower cylindrical layer, respectively. The slight increase in the interlamellar spacing (29.5 nm) of the lamellar layer on the prepattern, compared to its bulk value (λ_L = 28.3 nm), might be attributed to the aforementioned process of minimizing interfacial energy between lamellar and hexagonal layer, tending to be close to the principal spacing of hexagonal layer, λ_C = 33.7 nm.

We have just shown that the hexagonal prepattern can direct the lamellar orientation perpendicular to the substrate. As seen in Fig. 1, the distinct difference between the surface effect of hexagonal prepattern and that of the conventional neutral layer is that the former can induce not only the orientation of lamellar planes perpendicular to the substrate but also the alignment of lamellar planes along the (100) direction in the hexagonal lattice of the underlying prepattern. The surface effect of the hexagonal prepattern on the lamellar orientation, however, results in only local orientation due to the rotational symmetry of hexagonal lattice, i.e., the three degenerate states with respect to the lamellar (local) orientations are equally probable. Nevertheless, as will be shown below, this locally oriented but poor-aligned lamellae can be reformed effectively to have a near-perfect order when they are assembled within a trench (even in a micrometer-wide trench) introduced on the

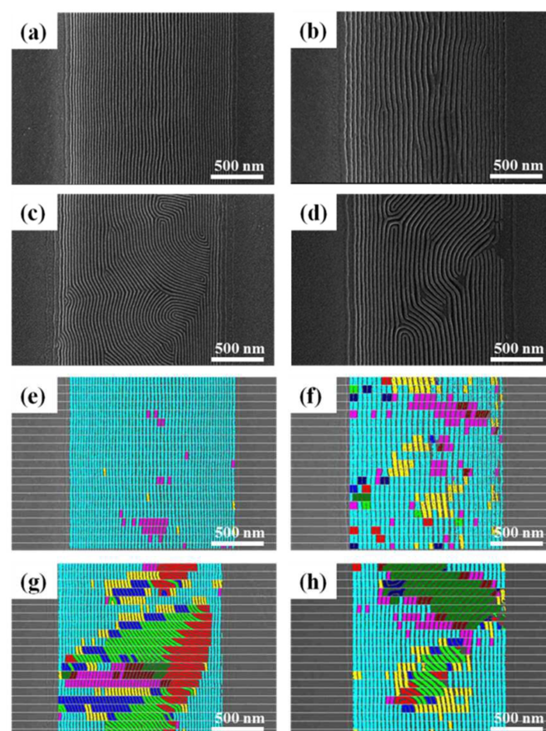

Fig. 2. SEM images of lamellar morphologies assembled within the 1.5-μm wide microgrooves and their image analysis via score distribution with respect to the degree of alignment. (a) and (b) correspond to SEM images for the PS-*b*-PMMA lamellae (thickness of ~ 230 nm) with M_n = 51 kg/mol and 75 kg/mol on the hexagonal prepatterns, respectively and (c) and (d) correspond to SEM images for the PS-*b*-PMMA lamellae with M_n = 51 kg/mol and 75 kg/mol on the neutral layers, respectively. (e)-(h) represent the image analysis results (i.e., the distribution of "alignment" pixels for the lamellae) for (a)-(d). In this case, the local regions of the alignment parallel to the sidewalls (F_o = 1.0) are colored cyan, whereas the regions of misalignment are colored other colors. As a result, the degree of lamellar alignment correspond to F_o = 0.96 (e), 0.73 (f), 0.39 (g), and 0.58 (h).

hexagonal prepattern

Fig. 2a and 2b show the SEM images of lamellar morphologies formed in the 1.5-μm-wide trench with two PMMA-selective sidewalls on the hexagonal prepattern, which are compared with those on the neutral layer (Fig. 2c and 2d, also see Fig. S3). In the case of PS-*b*-PMMA lamellae with λ_L = 28.3 nm (M_n = 51 kg/mol) on the hexagonal prepattern, well-aligned stripe pattern consisting of 54 lines is clearly seen between the sidewalls of the 1.5-μm-wide trench (Fig. 2a), whereas the orientational order is apparently poorer for the same system but on the neutral brush (Fig. 2c). The enhancement in orientational order is also evident for PS-*b*-PMMA with a larger period (λ_L = 38.1 nm, M_n = 75 kg/mol) on the hexagonal prepattern (Fig. 2b) when compared with the pattern on the neutral brush (Fig. 2d). The alignment of lamellae patterns was also examined by grazing-incidence small-angle X-ray scattering (GISAXS). During the measurement, the sample was rotated to adjust the beam direction as 0°, 30°, 60°, and 90°, with respect to the lamellar alignment. Consequently, it was observed that the intensity of first-order reflections significantly decreases as the angle between the beam direction and the lamellar alignment increases (Fig. S4), clearly indicating that there are not many multiple grains of the microdomains and a well-defined lamellar alignment is maintained over the large area of the sample. Furthermore, the internal structure of sample in Fig. 2a

Soft Matter Accepted Manuscript

was examined by cross-sectional SEM (Fig. S5). In this case, it can be clearly seen that the vertically oriented lamellar microdomains were apparent throughout the thickness, and the thin layer of underlying hexagonal patterns can be identified underneath of lamellar films.

To quantify the degree of lamellar alignments, we estimated the number fraction of the pixels in the "alignment" microstate (F_o) in the SEM images (Fig. 2e-2h), where the local regions of non-parallel stripe orientations or misalignments are colored (other than cyan representing the alignment parallel to the sidewalls) on the SEM images. For the image analysis, we selected at least five different SEM images (1.5 μm × 2.5 μm) from 2-3 different samples to obtain the averaged F_o values. The lamellar patterns in the SEM images were divided into a number of segments along the sidewall with ~75 nm length to estimate the tilt angle with respect to the sidewall.[46] The aligned microstate was defined as an image unit containing a segmented domain (PS)

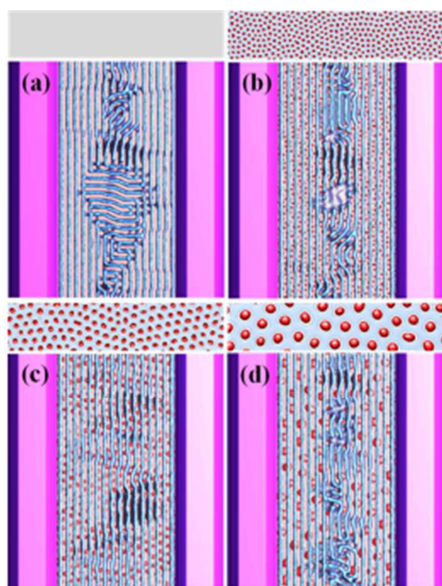

Fig. 3. (a) The CHC-LG-MDFT simulated images of lamellae in trench (a) on the neutral substrate, (b) on the hexagonal prepattern with $\lambda_C = 0.5\lambda_L$, (c) on the hexagonal prepattern with $\lambda_C = 1.0\lambda_L$, (d) on the hexagonal prepattern with $\lambda_C = 2.0\lambda_L$. In (a)-(d), regions of A-rich ($\Psi(\mathbf{r}) > 0$) and B-rich ($\Psi(\mathbf{r}) < 0$) domains in the upper lamellar layer are colored translucent maroon and opaque blue, respectively, whereas regions of A-rich (dots) and B-rich domains (matrix) in the underlying hexagonal prepatterns are colored opaque maroon and translucent blue, respectively, for visual clarification. The A-selective sidewalls are represented by pink color. The images in the upper panels represent the hexagonal prepatterns on which the lamellae are assembled.

parallel to the sidewall. To determine the aligned microstate among segmented domains, the angle tolerance for declaring aligned microstate is set to be $|\phi| \leq 5^o$, where ϕ is the angle between the line connecting the percolation point and the tangential vector of the sidewall. We assigned the cyan color for pixels having the tilt angle within 5° with respect to the sidewall, whereas the other colors were assigned for pixels with the tilt angle greater than 5°, indicating the misalignment. The degree of lamellar alignments, F_o, was calculated based on the areal fraction of cyan-color region relative to the total area of colored domains. As a result, the image analysis reveal that the lamellar alignment by the selective sidewall is more effective on the hexagonal prepattern than on the neutral brush, as shown in Fig. 2e-2h. In particular, the PS-*b*-PMMA lamellae with λ_L = 28.3 nm on the hexagonal pattern show near-perfect alignment with F_o = 0.96 (unity being perfect alignment), which is 2.5 times larger in F_o than the lamellar alignment on neutral brush (F_o = 0.39). In addition, we also examined the alignment of lamellar patterns at different thickness levels after reactive ion etching. After etching with different etching conditions, the residual thicknesses of overlying lamellar layers were adjusted as 140 nm, 130 nm, 40 nm, and 3 nm (Fig. S6). Consequently, it was clearly observed that the alignment of lamellae maintains at all thickness levels, successfully demonstrating a high degree of fidelity of our strategy.

To better understand this combined epitaxial assembly of BCP, we also simulated a model system of diblock lamellae (consisting of A- and B-block) on the hexagonal pattern in trench geometry by employing a mesoscale density functional theory (MDFT). For the simulation, we numerically integrate the Cahn-Hilliard-Cook (CHC) diffusion equation[47, 48] with the Landau-Ginzburg (LG) free energy[49-51] and the surface free energy (due to the bounding surfaces of BCP) where both the conformational contributions of BCP and the pairwise interactions between BCP and surface components are taken into account. Using the CHC-LG density functional method, thin films of symmetric BCP with the film thickness $\Delta = 2.5\ \lambda_L$ on the hexagonal prepatterns having the principal spacing in the range of $0.5\lambda_L \leq \lambda_C \leq 2.0\lambda_L$ were simulated between two

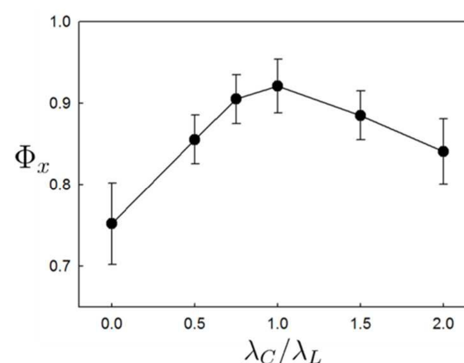

Fig. 4. The degree of lamellar alignment Φ_x as a function of λ_C/λ_L.

sidewalls with the separation distance $W = 16\ \lambda_L$. (The details of the simulation methods and the setup are described in the Experiment and Simulation section.)

Fig. 3a-3d presents the simulated images of lamellae between two selective sidewalls on the neutral substrate (Fig. 3a) and on the hexagonal patterns with $\lambda_C = 0.5\lambda_L$ (Fig. 3b), $\lambda_C = 1.0\lambda_L$ (Fig. 3c), and $\lambda_C = 2.0\lambda_L$ (Fig. 3d), respectively. For Fig. 3, the regions of A-rich ($\Psi(\mathbf{r}) > 0$) and B-rich ($\Psi(\mathbf{r}) < 0$) domains in the upper lamellar layer are colored translucent maroon and opaque blue, respectively, whereas regions of A-rich (dots) and B-rich domains (matrix) in the underlying hexagonal prepatterns are colored opaque maroon and translucent blue, respectively. In contrast to the case of experiment (Fig. 2), the effect of mismatch in the simulation was introduced by varying the domain size of underlying hexagonal patterns, while keeping the domain size (or M_n) of overlying lamellar patterns in order to isolate the mismatch effect from the kinetic effect. The simulation results show that the lamellar alignment on the hexagonal prepattern having $\lambda_C = 1.0\lambda_L$ are the best among the simulated cases, which bears out the experimental results that the hexagonal prepattern with $\lambda_C \approx \lambda_L$ enhances the lamellar alignment when coupled with graphoepitaxial assembly.

Soft Matter Accepted Manuscript

This journal is © The Royal Society of Chemistry 2015

In Fig. 4, the degree of lamellar alignment, Φ_x, is plotted as a function of λ_c/λ_L, where Φ_x is quantified from the "broken bonds" formula by[52]

$$\Phi_x = n_x/(n_x + n_y + n_z) \quad (1)$$

Here n_x is the number of the broken bonds (corresponding to the lamellar interface) in the direction normal to the sidewall (x-direction), and n_y and n_z are the number of the broken bonds in y- and z- direction, respectively. The numbers of broken bonds in each direction were estimated from the local A-monomer fraction $\Psi(\mathbf{r}) = \varphi(\mathbf{r}) - f$ (See Eq. (2) in Simulation section), where $\varphi(\mathbf{r})$ and f is the local volume fraction of A-monomer at the simulation grid point **r** and the mean fraction of A-monomer, respectively. Since $\Psi(\mathbf{r})$ changes the sign from negative (positive) to positive (negative) at the A/B interface, the numbers of broken bonds can be computed by counting the number of sign changes in each direction. The broken bonds formula (Φ_x) estimates the number of the interfacial points in x direction (perpendicular to the sidewall direction) relative to that of the total interfacial points in the simulation grids. Therefore, Φ_x is qualitatively same as F_o in that Φ_x also corresponds to the areal fraction of the simulation cells that two dissimilar domains are next to each other in x direction (so that segmented domains aligned along the surface direction). The estimation of Φ_x from simulation uses higher resolution than that of F_o from the image analysis. It should be also noted that the both estimation methods gives the similar quantity with the evaluation by the orientational factor (the second order Legendre polynomial) that can be obtained from the scattering profile, particularly when domains are strongly segregated.

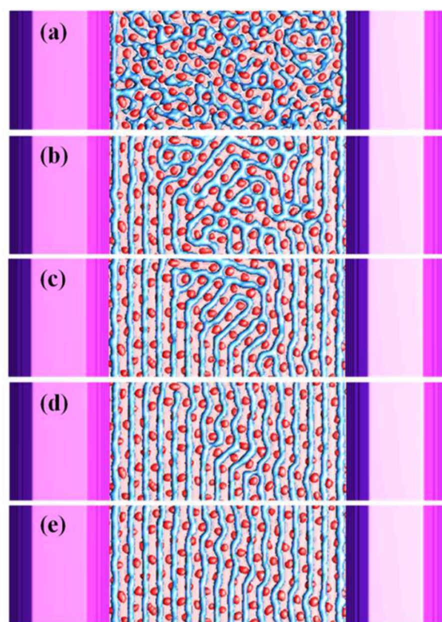

Fig 5. The time-evolution of the lamellar alignment at the film depth (z = 0.93Δ) near the hexagonal prepattern with λ_c/λ_L = 1.0 at the annealing time (a) t = 1 × 10^3δt, (b) t = 1 × 10^5δt, (c) t = 2 × 10^5δt, (d) t = 3 × 10^5δt, and (e) t = 4 × 10^5δt. (δt is the unit time step in the simulation.) In (a)-(d), the regions of A-rich and B-rich domains in the upper lamellar layer are colored translucent maroon and opaque blue, respectively, whereas regions of A-rich (dots) and B-rich domains (matrix) in the underlying hexagonal prepatterns are colored opaque maroon and translucent blue, respectively. The A-selective sidewalls are represented by pink color.

From Fig. 4, the Φ_x curve clearly indicates that the hexagonal prepattern (λ_c/λ_L > 0) assists the graphoepitaxial lamellar alignment as compared to the poorer lamellar alignment on the neutral substrate (λ_c/λ_L = 0) which relies only on the graphoepitaxial assembly driven from the sidewalls. The maximum alignment is found at λ_c/λ_L = 1.0, where the interfacial area between the phase-separating components at the boundary between lamellar and hexagonal layer is minimized. It is also worth noting that the multilayers in this work have a lattice mismatch between underlying hexagonal layer and overlying lamellar layer. In fact, the lattice mismatch in this system is caused both by the difference in intrinsic domain size between the hexagonal and lamellar layers, and also by random orientation of the hexagonal lattice with respect to the sidewall direction. While the former, characterized by λ_c/λ_L, is rather close to the lattice-match condition λ_c/λ_L = 1, the orientation of the hexagonal lattice is random with respect to the sidewall direction because of our experimental setup as well as the lattice defects. The simulation was also modeled to take into account the lattice mismatch between two layers, simulating the lamellar assembly on the randomly-oriented hexagonal lattice in the range of λ_c/λ_L = 0.5 ~ 2.0 with many lattice defects. Among these simulated lattice mismatch cases, the best orientational order was obtained at the λ_c/λ_L = 1 as shown in Fig. 4, where the error bars (obtained from independent simulations using different underlying hexagonal layers) reflects partly the effect of randomness in hexagonal orientations. Also, it can be expected that the periodic fluctuations induced by the (mismatched) hexagonal pattern can affect the graphoepitaxial lamellar assembly, being in harmony or in conflict with lamellar lattice parameter depending on the local situation. However, such chemo-induced periodic fluctuations are rather weakly fluctuating fields, compared to the strong fluctuating fields generated by the selective interaction from the sidewall, due to the weakly repelling interaction force between PS and PMMA. The weak interaction between PS and PMMA plays a role in easy changes among three quantized local orientational states, being ready to follow the strong compositional fluctuations developed from the sidewall. We also investigated the degree of lamellar alignment Φ_x as a function of the trench width W (Fig. S7). It is noted that although both Φ_x –W curves in the investigated range are in the way in sigmoidal curve, the Φ_x for the hexagonal prepattern is always larger than the neutral case. This clearly indicates that the sidewall effect is extended to a larger distance when the hexagonal prepattern is introduced.

Fig. 5 presents the time-evolution of the lamellar assembly at the film depth (z = 0.93Δ) near the hexagonal prepattern with λ_c/λ_L = 1.0, which demonstrates the dynamic pathway of graphoepitaxial lamellar alignment assisted by hexagonal pattern. In Fig. 5 , the regions of A-rich and B-rich domains in the upper lamellar layer are colored translucent maroon and opaque blue, respectively, whereas regions of A-rich (dots) and B-rich domains (matrix) in the underlying hexagonal prepatterns are colored opaque maroon and translucent blue, respectively. The A-selective sidewalls are represented by pink color. In the early stage of the lamellar assembly (Fig. 5a - 5b), the lamellar layers in the vicinity of the sidewalls are being propagated from the sidewalls, while the lamellar orientations in the mid-regions of the trench follow the local hexagonal orientations of the underlying prepattern, less affected by the distant sidewalls. The sidewall-driven, aligned lamellae are only wiggled slightly to avoid the unfavorable A/B contacts at the boundary between lamellar and hexagonal layer.

Soft Matter Accepted Manuscript

Meanwhile, the lamellae guided by the underlying hexagonal pattern are assembled independently in the middle of the trench, following one of three (100) directions in the local hexagonal lattice. The collisions between the fronts of these two lamellar propagation, which are from the sidewalls and from the (pattern-driven) nuclei in the middle of the trench, creates bent lamellar layers at the border of two lamellar growth (Fig. 5b). As the assembly proceeds further, the bent lamellae are reformed to be aligned by a zipping mechanism that the bend corners are sequentially swallowed by the lamellar layers developed from the sidewalls with an assistance of the underlying hexagonal pattern (Fig. 5b-5e). It is worth pointing out that the lamellar alignment via this zipping mechanism is more efficient on the hexagonal pattern that reduces a large number of orientational states of lamellar layers.

As a last aspect, it may be also necessary to consider the positioning of lamellar domain with respect to the underlying hexagonal domain, because our pattern analyses are focused on the orientational order of lamellae with respect to the sidewall direction. In fact, the thickness of lamellae within trench (~230 nm) is comparable to the trench height (~ 250 nm). Therefore, we could not directly observe the underlying cylindrical layers within trenches via electron microscopy due to thick overlying lamellar layers (Fig. 2a and 2b), whereas it was confirmed that the multilayers on the flat substrate, having much thinner lamellar films (~ 20 nm), exhibit a remarkable positional match between hexagonal and lamellar domains (Fig. 1a). However, the simulated morphology at the deep film depth near the hexagonal pattern (Fig. 5e) suggests that the aligned lamellae by the sidewall interaction are also nicely registered on their corresponding hexagonal domains, finding a certain way to be in harmony with strong fluctuations developed from the sidewall.

Experimental

Synthesis of Crosslinkable PS-*b*-PMMA block copolymer

Thermally crosslinkable PS-*b*-PMMA BCP was synthesized via reversible addition fragmentation transfer (RAFT) polymerization. First, methyl methacrylate (50 g, 499 mmol), 2,2'-azobis(2-methylpropionitrile) (AIBN) (24 mg, 0.15 mmol), and RAFT agent (450 mg, 1.50 mmol) were mixed and degassed. The reaction was carried out 70 ℃ for 12 hr. The reaction product was then precipitated into cold methanol, resulting in PMMA-RAFT macroinitiator as a pink powder (M_n = 19,000 g/mol and PDI = 1.10). To add the cross-linkable block PMMA-RAFT (10 g), styrene (71.9 g), the Meldrum's acid containing monomer[43] (5.85 g), and AIBN (0.0082 g) were mixed and degassed. The reaction was carried out at 70 ℃ or 48 hr. The reaction product was then precipitation into cold methanol, resulting in cross-linkable PS-*b*-PMMA, as a pink powder (M_n = 61 000 g/mol and PDI = 1.09).

Preparation of BCP thin films & Micro trench pattern

Three lamellar forming PS-*b*-PMMA BCPs, M_n = 51 kg/mol ($f_{PS,volume}$ = 0.52) and 75 kg/mol ($f_{PS,volume}$ = 0.54), were purchased from Polymer Source Inc. To prepare the aligned BCP multi-layer films, a silicon wafer was first neutralized using thermally cross-linkable PS-*r*-PMMA random copolymer that has been reported previously[43]. 0.4 wt% of thermally crosslinkable PS-*r*-PMMA solution in toluene was spin coated on a 6 inch silicon wafer (3000 rpm 120 sec). The coated silicon wafer thermally cross-linked under N_2 condition for 10 min. To prepare the multilayer structure, on top of the neutral layer, the cross-linkable PS-*b*-PMMA BCP was spin coated with 35 nm thickness. Thin films of lamella forming PS-*b*-PMMA BCPs were prepared on the micro-patterned substrates by spin-casting of toluene solutions. By adjusting the BCP concentration in toluene, the thicknesses were controlled from 60 to 230 nm. Films were annealed at 190 ℃ for 12 hr (crosslinkable BCP) or 250 ℃ for 48 hr (lamellar forming BCPs). To fabricate the trench pattern on top of the cylindrical layer were subsequently cross-linked at 250 ℃ for 10 min under inert N2 condition. The linear micro pattern was prepared using i-line photolithography process with a negative photoresist (SU-8) on top of the neutral or cross-linked cylindrical layer. To remove the PMMA block of lamellar pattern, the reactive ion etching (RIE system SNTEK) mode was operate with Ar (3 sccm)/ O_2 (15 sccm) by a RF power of 20 W at 0.1 torr. The etch rates for PMMA and PS are ~7.0 nm/sec and ~1.2 nm/sec, respectively. Also, it should be noted that this RIE condition can selectively remove the PS and PMMA polymer layers without affecting the SiO_2 substrates. To secure the reproducibility of the aligning lamella pattern, the same procedure repeated 3 or more times.

Characterizations

Characterizations: All commercially obtained reagents and solvents were used without further purification. Gel permeation chromatography (GPC) was handled in THF on a Waters Corp. supplied with a refractive index detector. Molecular weights and PDI of polymers were calculated relative to the standard linear polystyrene. Mass spectral data were assembled on a Micromass QTOF2 Quadrupole/Time-of Flight Tandem mass spectrometer (ESI-MS). At the Pohang Accelerator Laboratory (PAL) 9A and 3C beamlines in Korea, grazing-incidence small-angle X-ray scattering (GISAXS) experiments were carried out. A CCD detector that was installed controllable the sample to detector distance (SDD) was used to record 2D GISAXS patterns. The detector was located at the end of a vacuum guide tube where the X-ray (wavelength of 1.11 Å) passed through the sample.

Simulation

Simulation: The time evolution of the morphological structure of a molten AB diblock lamellae on the hexagonal prepattern in trench geometry is simulated by Landau-Ginzburg approach on the basis of a Cahn-Hilliard-Cook (CHC) diffusion equation:[47-51]

$$\frac{\partial \Psi(\mathbf{r})}{\partial t} = M\nabla^2 \left[\frac{\partial (F+F_{surf})}{\partial \Psi}\right] + \xi(\mathbf{r},t) \qquad (2)$$

Here the order parameter $\Psi(\mathbf{r})$ describes the deviation of local A-monomer fraction from its average value at a position r (defined by $\Psi(\mathbf{r}) = \varphi(\mathbf{r}) - f$ where $\varphi(\mathbf{r},\mathrm{t})$ and f are the local volume fraction of A-monomer and the mean fraction of A-monomer), M is a mobility constant, F is the free energy of the mesophase formed by diblock copolymer, F_{surf} is the free energy associated with interaction between block copolymer and its bounding surface (hexagonal pattern, sidewalls, free surface), and ξ represents the thermal noise satisfying the fluctuation dissipation theorem.

The free energy of mesophase has a functional form, $F \equiv F[(\Psi(r)]$, given approximately by Landau-Ginzburg free energy:[49-51]

Soft Matter Accepted Manuscript

This journal is © The Royal Society of Chemistry 2015

$$F \cong \int d\mathbf{r}\left[-\frac{\tau}{2}\Psi^2(\mathbf{r}) + \frac{\mu}{3!}\Psi^3(\mathbf{r}) + \frac{\eta}{4!}\Psi^4(\mathbf{r}) + \frac{D}{2}(\nabla\Psi)^2\right] + \frac{b}{2}\int d\mathbf{r}\int d\mathbf{r}' G(\mathbf{r}-\mathbf{r}')\Psi(\mathbf{r})\Psi(\mathbf{r}') \quad (3)$$

Here τ is a temperature-like parameter related to the Flory interaction parameter between A- and B-monomer (χ), and μ, η, and D are related to the architecture of block copolymer determining conformational contributions when the block copolymers are packed into a certain type of mesophase. The last term represents a long-range repulsion penalizing long-wavelength inhomogeneity through the Green function G with a period-controlling parameter b where $G(\mathbf{r}-\mathbf{r}')$ satisfies $\nabla G(\mathbf{r}-\mathbf{r}') = -\delta(\mathbf{r}-\mathbf{r}')$. The surface free energy F_{surf} is given as

$$F_{surf}(\Psi) = \int d\mathbf{r} s(\mathbf{r})\Psi(\mathbf{r}) \quad (4)$$

where $s(\mathbf{r})$ is a surface field proportional to the difference in surface/polymer interfacial tension between surface/A-block and surface/B-block and nonzero only at the position next to the boundary surface if the surface attracts one of the blocks ($s< 0$ if the surface is attractive to A-block and vice versa). The molecular parameters τ, μ, η, D, and b for diblock architecture can be approximately given as

$$\tau = 2(\chi - \chi_s) + \frac{3^{1/2}}{N\, f^{3/2}(1-f)^{3/2}}, \mu = \frac{\Gamma_3}{N}, \eta = \Gamma_4(0,0)/N \quad (5)$$

$$D = \frac{1}{12f(1-f)}, b = \frac{9}{N^2 f^2 (1-f)^2} \quad (6)$$

where χ_s is the χ at the spinodal, N is the chain length of diblock copolymer in unit of segmental length, Γ_3 and $\Gamma_4(0,0)$ are Leibler vertex functions computed from the monomer correlation functions.[44, 53, 54] The CHC diffusion equation of eq (2) is numerically integrated in the discrete space with $\mathrm{W} \times \mathrm{y} \times \Delta = 100a \times 200a \times 20a$ where W is the width of trench, y is the transverse dimension, Δ is the film thickness, and a is the unit spacing of the simulation grids. The time t is in unit of a^2/M where a and M are set to be unity. For the underlying hexagonal prepattern, we set $f = 0.3$ and $\chi N = 16$ for CHC equation and equilibrate a hexagonal morphology. The graphoepitaxial assembly of lamella-forming BCP was then simulated on the prepared hexagonal pattern by setting $f = 0.3$ and $\chi N = 16$. The reflection boundary conditions are used at the boundary with sidewalls and with the free surface of the film whereas Dirichlet boundary condition is used at the boundary between the hexagonal pattern and the lamellar film.

Conclusions

In summary, we demonstrate an efficient method for fabricating aligned line patterns using graphoepitaxial assembly of BCP lamellae on hexagonal prepattern. It is found from both experiment and simulation that the hexagonal prepattern can assist the graphoepitaxial assembly of lamellar alignment as compared to the lamellar alignment on the neutral substrate even though the underlying hexagonal pattern contains structural defects. The maximum enhancement in the degree of lamellar alignment was achieved when the principal domain spacing of underlying hexagonal pattern is comparable to that of the upper lamellar layer. While there have been enormous studies on the DSA processes (i.e., graphoepitaxy or chemoepitaxy), not many examples can be found on the combination of two techniques. In this work, we successfully demonstrate the synergetic effect of these two methods by overcoming their inherent limitations. In this regards, our approach can provide an important platform for DSA process that can meet the industrial specifications such as a high-fidelity and cost-effective processing over large area.

Acknowledgements

This work was by National Research Foundation of Korea grant funded by the Korea government (MSIP) (No. 2012M3A7B4035323) and also by the Global Frontier R&D Program (No. 2013M3A6B1078869) on Center for Hybrid Interface Materials (HIM) funded by the Ministry of Science, ICT & Future Planning. H.J., S.W., and J.B. also acknowledge the support by the Human Resources Development Program of KETEP grant (No. 20134010200600) funded by the Korea government Ministry of Trade, Industry and Energy.

Notes and references

[a] Department of Chemical and Biological Engineering, Korea University, Seoul 136-713, Republic of Korea. E-mail: junehuh@korea.ac.kr, joona@korea.ac.kr
[b] Department of Chemical and Biolomolecular Engineering, Yonsei University, Seoul 120-749, Republic of Korea.
[c] LCD R & D Center, Samsung Electronics San#24 Nongseo-dong, Giheung-gu, Yongin-city, Gyeonggi-do 446-711, Republic of Korea.
[d] Department of Chemical Engineering, Pusan National University, Kumjeong-ku, Busan 609-735, Republic of Korea.
[e] Photo-Electronic Hybrids Research Center, Korea Institute of Science and Technology (KIST), Seoul 136-791, Republic of Korea.

† Electronic Supplementary Information (ESI) available: Synthetic schematic of crosslinkable PS-*b*-PMMA, SAXS profiles and SEM images See DOI: 10.1039/b000000x/

1. J. Bang, U. Jeong, D. Y. Ryu, T. P. Russell and C. J. Hawker, *Adv. Mater.*, 2009, **21**, 4769-4792.
2. C. T. Black, *Nat. Nanotechnol.*, 2007, **2**, 464-465.
3. C. T. Black, *ACS Nano*, 2007, **1**, 147-150.
4. C. J. Hawker and T. P. Russell, *MRS Bull.*, 2005, **30**, 952-966.
5. S. Y. Yang, I. Ryu, H. Y. Kim, J. K. Kim, S. K. Jang and T. P. Russell, *Adv. Mater.*, 2006, **18**, 709-712.
6. S. Horiuchi, T. Fujita, T. Hayakawa and Y. Nakao, *Langmuir*, 2003, **19**, 2963-2973.
7. T. Thurn-Albrecht, J. Schotter, G. A. Kästle, N. Emley, T. Shibauchi, L. Krusin-Elbaum, K. Guarini, C. Black, M. T. Tuominen and T. P. Russell, *Science*, 2000, **290**, 2126-2129.
8. M. J. Fasolka and A. M. Mayes, *Ann. Rev. Mater. Res.*, 2001, **31**, 323-355.
9. C. T. Black, R. Ruiz, G. Breyta, J. Y. Cheng, M. E. Colburn, K. W. Guarini, H.-C. Kim and Y. Zhang, *IBM J. Res. Dev.*, 2007, **51**, 605-633.
10. R. A. Segalman, *Mat. Sci. Eng. R*, 2005, **48**, 191-226.

Soft Matter Accepted Manuscript

11. J. Bang, S. H. Kim, E. Drockenmuller, M. J. Misner, T. P. Russell and C. J. Hawker, *J. Am. Chem. Soc.*, 2006, **128**, 7622-7629.
12. J. G. Lee, Y. S. Jung, S. H. Han, K. M. Kim and Y. K. Han, *Adv. Mater.*, 2014, **26**, 2894-2900.
13. H.-C. Kim, S.-M. Park and W. D. Hinsberg, *Chem. Rev.*, 2009, **110**, 146-177.
14. J. Y. Cheng, C. T. Rettner, D. P. Sanders, H.-C. Kim and W. D. Hinsberg, *Adv. Mater.*, 2008, **20**, 3155-3158.
15. R. Ruiz, R. L. Sandstrom and C. T. Black, *Adv. Mater.*, 2007, **19**, 587-591.
16. H.-S. Moon, D. O. Shin, B. H. Kim, H. M. Jin, S. Lee, M. G. Lee and S. O. Kim, *J. Mater. Chem.*, 2012, **22**, 6307-6310.
17. R. A. Segalman, K. E. Schaefer, G. H. Fredrickson, E. J. Kramer and S. Magonov, *Macromolecules*, 2003, **36**, 4498-4506.
18. R. A. Segalman, A. Hexemer and E. J. Kramer, *Macromolecules*, 2003, **36**, 6831-6839.
19. J. K. Yang, Y. S. Jung, J.-B. Chang, R. Mickiewicz, A. Alexander-Katz, C. Ross and K. K. Berggren, *Nat. Nanotechnol.*, 2010, **5**, 256-260.
20. S.-M. Park, X. Liang, B. D. Harteneck, T. E. Pick, N. Hiroshiba, Y. Wu, B. A. Helms and D. L. Olynick, *ACS Nano*, 2011, **5**, 8523-8531.
21. M. R. Hammond, E. Cochran, G. H. Fredrickson and E. J. Kramer, *Macromolecules*, 2005, **38**, 6575-6585.
22. M. R. Hammond and E. J. Kramer, *Macromolecules*, 2006, **39**, 1538-1544.
23. W. I. Park, K. Kim, H.-I. Jang, J. W. Jeong, J. M. Kim, J. Choi, J. H. Park and Y. S. Jung, *Small*, 2012, **8**, 3762-3768.
24. J. W. Jeong, W. I. Park, L. M. Do, J. H. Park, T. H. Kim, G. Chae and Y. S. Jung, *Adv. Mater.*, 2012, **24**, 3526-3531.
25. B. H. Kim, S. J. Park, H. M. Jin, J. Y. Kim, S.-W. Son, M. H. Kim, C. M. Koo, J. Shin, J. U. Kim and S. O. Kim, *Nano Letters*, 2015, **15**, 1190-1196.
26. B. H. Kim, Y. Choi, J. Y. Kim, H. Shin, S. Kim, S. W. Son, S. O. Kim and P. Kim, *Adv. Mater.*, 2014, **26**, 4665-4670.
27. S.-J. Jeong, J. Y. Kim, B. H. Kim, H.-S. Moon and S. O. Kim, *Materials Today*, 2013, **16**, 468-476.
28. S. M. Park, M. P. Stoykovich, R. Ruiz, Y. Zhang, C. T. Black and P. F. Nealey, *Adv. Mater.*, 2007, **19**, 607-611.
29. J. Y. Cheng, A. M. Mayes and C. A. Ross, *Nat. Mater.*, 2004, **3**, 823-828.
30. E. W. Edwards, M. F. Montague, H. H. Solak, C. J. Hawker and P. F. Nealey, *Adv. Mater.*, 2004, **16**, 1315-1319.
31. S. O. Kim, H. H. Solak, M. P. Stoykovich, N. J. Ferrier, J. J. de Pablo and P. F. Nealey, *Nature*, 2003, **424**, 411-414.
32. E. W. Edwards, M. Müller, M. P. Stoykovich, H. H. Solak, J. J. de Pablo and P. F. Nealey, *Macromolecules*, 2007, **40**, 90-96.
33. E. W. Edwards, M. P. Stoykovich, H. H. Solak and P. F. Nealey, *Macromolecules*, 2006, **39**, 3598-3607.
34. R. Ruiz, H. Kang, F. A. Detcheverry, E. Dobisz, D. S. Kercher, T. R. Albrecht, J. J. de Pablo and P. F. Nealey, *Science*, 2008, **321**, 936-939.
35. M. P. Stoykovich, M. Müller, S. O. Kim, H. H. Solak, E. W. Edwards, J. J. De Pablo and P. F. Nealey, *Science*, 2005, **308**, 1442-1446.
36. C.-C. Liu, A. Ramírez-Hernández, E. Han, G. S. Craig, Y. Tada, H. Yoshida, H. Kang, S. Ji, P. Gopalan and J. J. de Pablo, *Macromolecules*, 2013, **46**, 1415-1424.
37. D. P. Sanders, J. Cheng, C. T. Rettner, W. D. Hinsberg, H.-C. Kim, H. Trung, A. Fritz, S. Harrer, S. Holmes and M. Colburn, *J. Photopolym. Sci. Technol.*, 2010, **23**, 11-18.
38. C.-C. Liu, P. F. Nealey, A. K. Raub, P. J. Hakeem, S. R. Brueck, E. Han and P. Gopalan, *J. Vac. Sci. Technol. B*, 2010, **28**, C6B30-C36B34.
39. P. A. R. Delgadillo, R. Gronheid, C. J. Thode, H. Wu, Y. Cao, G. Lin, M. Somervell, K. Nafus and P. F. Nealey, *J. Photopolym. Sci. Technol.*, 2012, **25**, 77-81.
40. H. Jung, D. Hwang, E. Kim, B.-J. Kim, W. B. Lee, J. E. Poelma, J. Kim, C. J. Hawker, J. Huh, D. Y. Ryu and J. Bang, *ACS Nano*, 2011, **5**, 6164-6173.
41. F. A. Leibfarth, M. Kang, M. Ham, J. Kim, L. M. Campos, N. Gupta, B. Moon and C. J. Hawker, *Nat. Chem.*, 2010, **2**, 207-212.
42. F. A. Leibfarth, Y. Schneider, N. A. Lynd, A. Schultz, B. Moon, E. J. Kramer, G. C. Bazan and C. J. Hawker, *J. Am. Chem. Soc.*, 2010, **132**, 14706-14709.
43. H. Jung, F. A. Leibfarth, S. Woo, S. Lee, M. Kang, B. Moon, C. J. Hawker and J. Bang, *Adv. Funct. Mater.*, 2013, **23**, 1597-1602.
44. G. H. Fredrickson, *Macromolecules*, 1987, **20**, 2535-2542.
45. G. Pickett, T. Witten and S. Nagel, *Macromolecules*, 1993, **26**, 3194-3199.
46. These segments have some percolated domains with the percolation points connecting from the upper side to the lower side of the subsection. The image analysis using MATLAB software for counting aligned microstates starts with finding a perimeter of morphological objects in binary image (black and white) to identify the connected lines and the percolation points, which is used for judging whether or not a specific percolated domain (microstate) is parallel to the sidewall direction.
47. S. Ren and I. Hamley, *Macromolecules*, 2001, **34**, 116-126.
48. Y. Oono and S. Puri, *Phys. Rev. A*, 1988, **38**, 434-453.
49. S. Qi and Z.-G. Wang, *Phys. Rev. E*, 1997, **55**, 1682-1697.
50. M. Pinna and A. Zvelindovsky, *Eur. Phys. J. B.*, 2012, **85**, 1-18.
51. J. Huh, J. Y. Jung, J. U. Lee, H. Cho, S. Park, C. Park and W. H. Jo, *ACS Nano*, 2010, **5**, 115-122.
52. T. Ohta, D. Jasnow and K. Kawasaki, *Phys. Rev. Lett.*, 1982, **49**, 1223-1226.
53. L. Leibler, *Macromolecules*, 1980, **13**, 1602-1617.
54. A. Mayes, M. Olvera de La Cruz and W. McMullen, *Macromolecules*, 1993, **26**, 4050-4051.

Soft Matter Accepted Manuscript

This journal is © The Royal Society of Chemistry 2015

Soft Matter RSCPublishing

PAPER

Graphical Abstract

In this work, we demonstrate the simple and feasible technology for DSA process by combining the graphoepitaxy with "inexpensive" chemoepitaxial assembly to improve the alignment of lamellar microdomains.

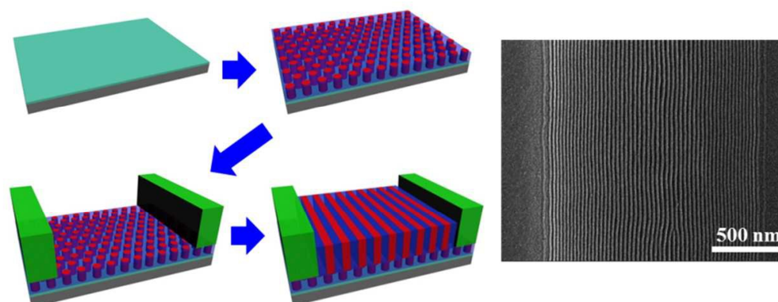

Soft Matter Accepted Manuscript